

pubs.acs.org/cm Article

# Wafer-Scale Anion Exchange Conversion of Nonlayered PtS Films to van der Waals Two-Dimensional PtTe<sub>2</sub> Layers with Negative Photoresponsiveness

Sang Sub Han, Mashiyat Sumaiya Shawkat, Yoong Hee Lee, Gyehyun Park, Hao Li, Hee-Suk Chung, Changhyeon Yoo, Sohrab Alex Mofid, Shahid Sattar, Nitin Choudhary, Jea-Young Choi, YounJoon Jung, Jung Han Kim,\* and Yeonwoong Jung\*



Cite This: Chem. Mater. 2022, 34, 6996-7005



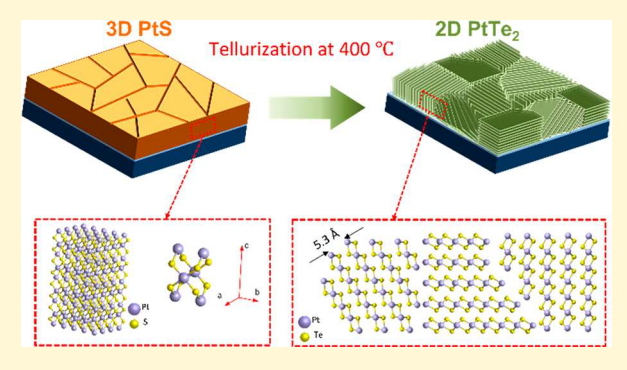
**ACCESS** 

III Metrics & More

Article Recommendations

Supporting Information

ABSTRACT: This study reports on the controlled vapor-phase anion exchange conversion of three-dimensional (3D) platinum(II) sulfide (PtS) thin films to two-dimensional platinum ditelluride (2D PtTe<sub>2</sub>) van der Waals (vdW) layers. The low temperature (i.e., 400 °C) thermal tellurization of chemical vapor deposition (CVD)-grown PtS thin films leads to the formation of 2D PtTe<sub>2</sub> vdW layers with a modulated crystallographic orientation, i.e., a mixture of horizontally and vertically oriented 2D layers. This chemical conversion enables the tunable electrical transport accompanying semiconducting-to-metallic transition as well as negative photoresponsiveness in the 2D PtTe<sub>2</sub> layers. Density functional theory (DFT) calculations verify the thermodynamic principle for the conversion in the frame of free energy



landscapes. The present work suggests a new chemical route for controlling the atomic and chemical structures of 2D transition metal dichalcogenides (TMDs) toward their wafer-scale modulation of electrical and opto-electrical properties.

# 1. INTRODUCTION

The extraordinary material properties of two-dimensional (2D) transition metal dichalcogenide (TMD) van der Waals (vdW) layers have continued to offer exciting opportunities for futuristic optoelectronic devices. 1-3 As a critical step to realize such device applications, their large-area growth and integration accompanying precision-tailored physical/chemical structures still pose a considerable challenge. 4-6 To this end, chemical vapor deposition (CVD)-based growth methods stand out due to their capability for dimensional scaling and heterogeneous manipulation of distinct chemical compo-The atomic/electronic structures of as-grown 2D TMD layers can be further tuned through various postgrowth chemical routes, achieving highly exotic yet modulated optoelectronic properties. The idea of chemically transforming materials for their optoelectronic property conversion has been extensively explored with materials of reduced dimensions, such as zero-dimensional (0D) nanocrystals and one-dimensional (1D) nanowires. Particularly, the ion exchange reaction, i.e., selective conversion of constituting ions, has been applied to develop a variety of metal chalcogenide-based nanostructures. In this approach, the cations/anions within postgrown nanomaterials are controllably substituted to a targeted degree, achieving modulated chemical transformations. The intrinsic advantages of this reaction method include the atomic

precision of chemical and physical integrities as well as the excellent versatility applicable to various geometries. For instance, compound semiconductor 0D nanocrystals and 1D nanowires with distinct electrical components (e.g., II-VI or III-V) have been demonstrated by controlled cation<sup>9</sup> or anion 10 exchange reactions. Furthermore, the method has been adopted for the synthesis of heterostructured nanocrystals and/or tuning their electrical properties via means of doping. 11,12 For instance, an earlier study shows a significant enhancement of the electrical conductivity and mobility of the host materials converted through such reactions as demonstrated in chalcogenide thin films. 13 Despite the vastly explored ion-exchange reactions in other low-dimensional materials, the controlled chemical and electrical conversions of 2D TMD layers have been rarely reported. So far, a few studies have suggested the intrinsic versatility and feasibility of ion-exchange reactions in these materials with limited  $(<\mu m^2)$  lateral dimensions. 14,15 However, the intrinsically scalable ion-

Received: May 13, 2022 Revised: July 11, 2022 Published: July 20, 2022





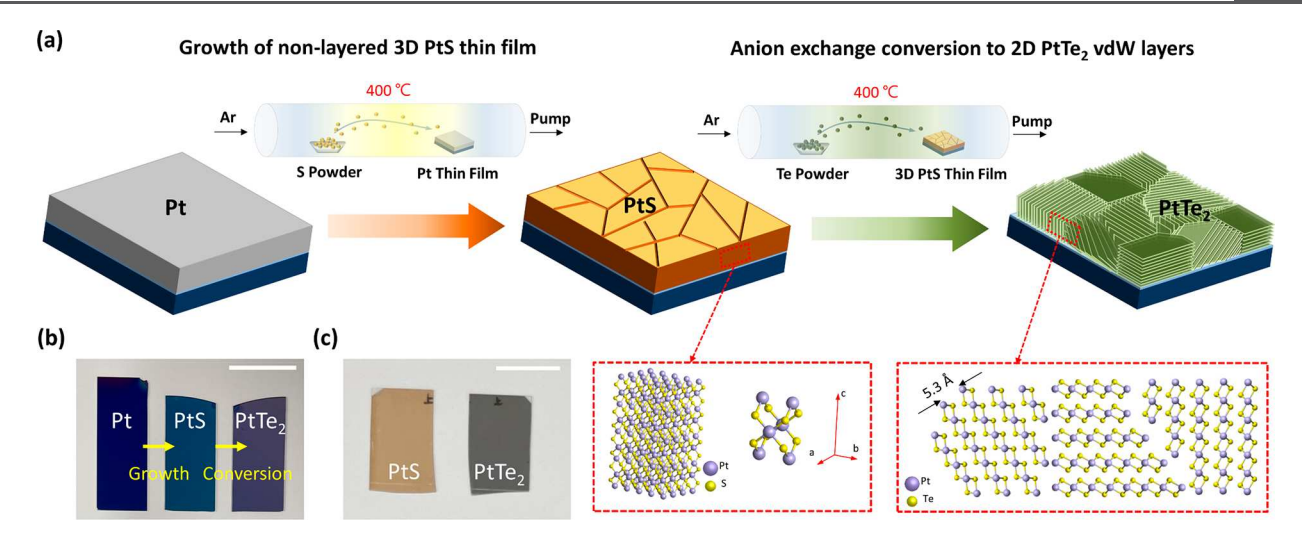


**Figure 1.** (a) Schematic depiction of the wafer-scale anion exchange conversion of 3D PtS films to 2D PtTe<sub>2</sub> layers. (b) Camera image of three different samples prepared on SiO<sub>2</sub>/Si wafers; i.e., as-deposited Pt, 3D PtS thin film sulfurized from Pt, and 2D PtTe<sub>2</sub> layers converted from 3D PtS, respectively. (c) Camera image of the 3D PtS film and converted 2D PtTe<sub>2</sub> layers prepared on willow glass substrates. The scale bars in (b) and (c) are 2 cm.

exchange conversion to acquire large-area (>cm²) 2D TMD layers of spatial/chemical homogeneity with modulated electrical properties has been hardly explored. Particularly, the vapor-phase ion-exchange reaction of "wafer-scale" 2D TMD layers beyond the conventionally adopted liquid-phase conversions of 0D and 1D nanomaterials has remained largely unavailable.

Herein, we report on the scalable conversion of covalently bonded platinum(II) sulfide (PtS) thin films into 2D platinum ditelluride (2D PtTe<sub>2</sub>) vdW layers through the controlled vapor-phase anion exchange reaction. 2D PtTe2 layers are known to exhibit extremely high electrical conductivity 16-19 and thickness-dependent bandgap tunability, 20,21 rendering many opportunities for electrical applications. While their synthesis has been explored through a variety of CVD reactions, 17,19,22,23 a chemical method to obtain them by directly converting pregrown materials has not yet been reported. To this end, we identified that the thermal tellurization at 400 °C uniformly transformed the CVDgrown PtS thin films of three-dimensional (3D) tetragonal structures into PtTe2 vdW layers of mixed 2D layer orientations with a dimension of > cm<sup>2</sup>. This chemical/ structural conversion also accompanied the modulation of electrical properties, leading to the transition of semiconducting-to-metallic carrier transports. The fundamental thermodynamic principle for this anion exchange reaction was understood in the frame of free energy landscapes, revealed by density functional theory (DFT) calculations. Furthermore, the converted 2D PtTe<sub>2</sub> layers interfaced with polyvinyl butyral (PVB) polymers exhibited intriguing "negative" photoresponsiveness—i.e., a decrease of photocurrent upon optical illumination—similar to the observations with graphene.

# 2. EXPERIMENTAL SECTION

**2.1. Growth of the PtS Film.** The PtS film was grown by the thermal sulfurization of the thin Pt films. Pt film of a controlled thickness of 3 nm was deposited on silicon dioxide/silicon (SiO<sub>2</sub>/Si) wafers and the salt substrate (sodium chloride, NaCl) by an e-beam evaporator (Thermionics VE-100) with a deposition rate of 0.05 Å/s. Pt-deposited samples were placed in the central heating zone of the horizontal quartz tube furnace (Lindberg/Blue M Mini-Mite), and the

alumina boats filled with precursor sulfur powder (99.5%, Millipore Sigma) were placed inside the tube at the upstream of the furnace. The quartz tube was pumped down to a pressure of 50 mTorr and then purged by ultrapure Ar gas (99.99%) to remove oxygen ( $O_2$ ) and organic residuals for 15 min. The furnace was subsequently heated to 400 °C in 50 min, and it was maintained at the growth temperature of 400 °C for the additional 50 min under a continuous supply of the Ar gas at a flow rate of 200 standard cubic centimeters per minute (sccm). After the additional 50 min of thermal-assisted PtS growth, the quartz tube was cooled down naturally to room temperature.

- **2.2. Preparation of PVB.** A total of 3 g of PVB powder was mixed with 20 g of pure ethyl alcohol, and the mixture was left under stirring for 3 h at room temperature at 400–500 rpm. The PVB dispersion was then drop-casted onto the 2D PtTe $_2$  layers/salt wafers placed inside a spin coater before spin-coating for 30 s, after which it was allowed to dry for 5–10 min at room temperature.
- 2.3. Transmission Electron Microscopy (TEM) and Energy-Dispersive X-ray Spectroscopy (XPS) Characterizations. All the samples were characterized by a high-resolution (HR) transmission electronic microscope (Talos F200X, Thermo Fisher Scientific) attached to an energy-dispersive X-ray spectrometer operating at an acceleration voltage of 200 kV. For the plane-view TEM characterization, a buffered oxide etchant (BOE) was directly applied to the SiO<sub>2</sub>/Si wafer together with as-grown samples, etching away the underlying SiO<sub>2</sub> layer. The delaminated samples were then transferred onto copper TEM grids with a lacey carbon support film and left to dry at room temperature overnight. For scanning transmission electronic microscopy (STEM) and EDS, cross-sectional TEM samples have been carried out in Dual-Beam focused ion beam (FIB) (Scios2, Thermo Fisher Scientific) applying the lift-out technique. As-grown samples on the SiO<sub>2</sub>/Si wafer were subsequently cross-sectioned using a 30 kV gallium (Ga) ion beam. X-ray photoelectron spectroscopy (XPS) characterizations for all samples were performed using ESCALAB 250 (Thermo Fisher Scientific) with an Al Kα-ray source (1486.3 eV) in an ultrahigh vacuum condition  $(10^{-9} \text{ mBar}).$
- **2.4. Electrical and Photocurrent Measurements.** All electrical measurements were carried out using a home-built probe station and a semiconductor parameter analyzer (HP 4156A). Photocurrent measurements were performed using optical illuminators of various wavelengths (625 nm; Thorlabs M625L4-C2, and 940 nm; Thorlabs M940L3-C1).
- **2.5. DFT Calculation.** First-principles calculations were performed with DFT and projector-augmented plane-wave methods <sup>25,26</sup> as implemented in the Vienna Ab-initio Simulation Package

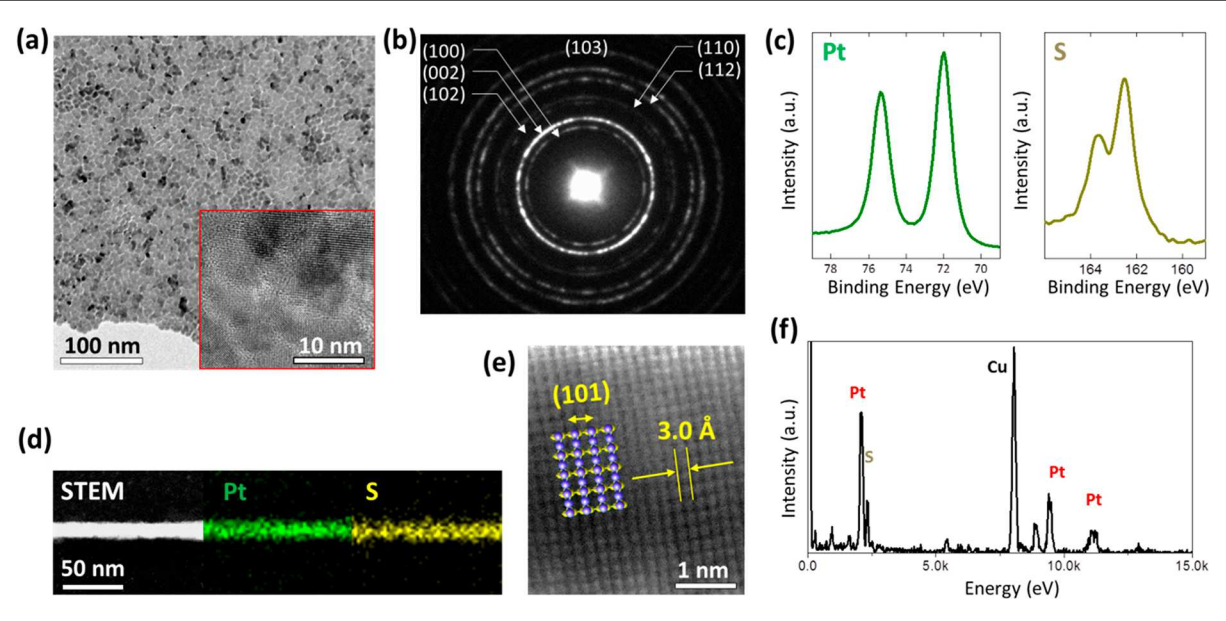


**Figure 2.** (a) Low-magnification plane-view TEM image of a PtS film and its corresponding HR-TEM image (inset). (b) SAED indexed pattern of the PtS film in (a). (c) XPS spectra of Pt 4f and S 2p core-level binding energies. (d) Cross-sectional EDS mapping images and (e) HR-STEM image of the PtS film. (f) EDS spectra profile obtained from the samples in (d) and (e).

(VASP).<sup>27</sup> To describe exchange and correlation effects, the generalized gradient approximation was used in the Perdew-Burke-Ernzerhof parametrization. A large plane wave cutoff energy of 450 eV was used to ensure the convergence of our results. In order to confirm dynamical stability, we calculated phonon band structures employing  $3 \times 3 \times 3$  and  $3 \times 3 \times 1$  supercells of bulk PtS and 2D PtTe2, respectively, using the Phonopy package.28 For the computation of Gibbs free energies and associated thermodynamic quantities at the given experimental conditions (T = 400 °C, P = 50mTorr), we used the VASP\_Gibbs package, which accurately determines free energies using frequency analysis.<sup>29</sup> We also performed DFT calculations for the system consisting of adsorbateattached vertically aligned 2D PtTe2 bilayers and identified influences of the adsorbates on their electronic structures. Two representative adsorbates of hydroxyl (OH) group and O2 molecules were employed. The plane wave cutoff energy was set to a sufficiently large value of 700 eV, and relaxation was performed until ensuring an energy convergence of  $10^{-6}$  eV and force convergence of  $10^{-2}$  eV/Å.

# 3. RESULTS AND DISCUSSION

Figure 1 demonstrates the anion exchange conversion of nonlayered 3D PtS films to vdW 2D PtTe<sub>2</sub> layers. Figure 1a illustrates the step-by-step conversion process, which initially originates from the growth of 3D PtS films. Pt thin films of controlled thickness are deposited on SiO<sub>2</sub>/Si wafers, and the Pt-deposited wafers are placed into a CVD chamber. The samples are then sulfurized at 400 °C under a controlled supply of vaporized S, which converts the Pt films to nonlayered 3D PtS films. Further details concerning the growth procedure are presented in the Experimental Section. The prepared 3D PtS thin films are converted to vdW 2D PtTe<sub>2</sub> layers through a controlled thermal tellurization process. The PtS thin films are transferred into another quartz tube furnace containing Te powder at the upstream side of the furnace. The quartz tube is pumped down to a pressure of 50 mTorr followed by purging with argon (Ar) gas. The furnace is ramped up to 400 °C in 50 min and is held at that temperature for another 50 min under a constant supply of Ar gas at a flow rate of 200 sccm. After the conversion, the furnace is allowed to cool down to room temperature at a natural cooling rate.

The insets in Figure 1a illustrate ball-and-stick unit cell models of an initial PtS thin film (middle) and converted 2D PtTe2 vdW layers (right). Before the conversion, the PtS film possesses a nonlayered covalently bonded tetragonal structure (space group:  $P4_2/mmc$ ) with lattice parameters of a = b = 3.50Å and c = 6.06 Å. The Pt atoms (purple balls) bonded to the tetrahedral sites of the S atoms (yellow balls) alternatively occupy face-centered (101) planes along the c axis.<sup>31</sup> This intrinsically "non-layered" 3D PtS film becomes converted to a "layered" 2D PtTe, structure bonded by vdW attraction with a uniform interlayer spacing (i.e., vdW gap) of 5.3 Å. The converted PtTe<sub>2</sub> layers possess a mixed-orientation of horizontally and/or vertically aligned individual 2D layersshown in detail in the later sections. Figure 1b shows camera images of three different samples prepared on SiO<sub>2</sub>/Si wafers; i.e., as-deposited Pt, 3D PtS thin film sulfurized from Pt, and 2D PtTe<sub>2</sub> layers converted from 3D PtS thin film. Figure 1c shows a camera image of the 3D PtS thin film and the converted 2D PtTe<sub>2</sub> layers prepared on an optically transparent willow glass substrate, exhibiting distinguishable optical colors.

Figure 2 presents structural and chemical characterizations of the as-prepared nonlayered PtS thin films before their anion exchange conversion, obtained by TEM and XPS. Figure 2a displays a representative low-magnification plane-view TEM image of a PtS film revealing its spatially homogeneous and continuous morphology. The HR-TEM image in the inset shows its polycrystalline structure with lattice fringes. Figure 2b presents a selected area electron diffraction (SAED) indexing of the sample, exhibiting multiple ring patterns belonging to the tetragonal PtS crystal with a space group of P4<sub>2</sub>/mmc.<sup>31</sup> Figure 2c presents XPS spectra obtained from the same sample investigated for the plane-view TEM/SAED analysis. Corelevel spectra of Pt 4f (left) and S 2p (right) binding energies are presented, revealing the binding energies of Pt  $4f_{5/2}$ , Pt  $4f_{7/2}$ , S  $2p_{1/2}$ , and S  $2p_{3/2}$  at 75.4, 72.0, 163.7, and 162.5 eV, respectively. The results are consistent with the previous observation for bulk PtS crystals, 30,33,34 and the atomic ratio of Pt:S calculated from the XPS spectra is ~56:44, indicating the stoichiometric growth of the PtS. Figure 2d shows a cross-

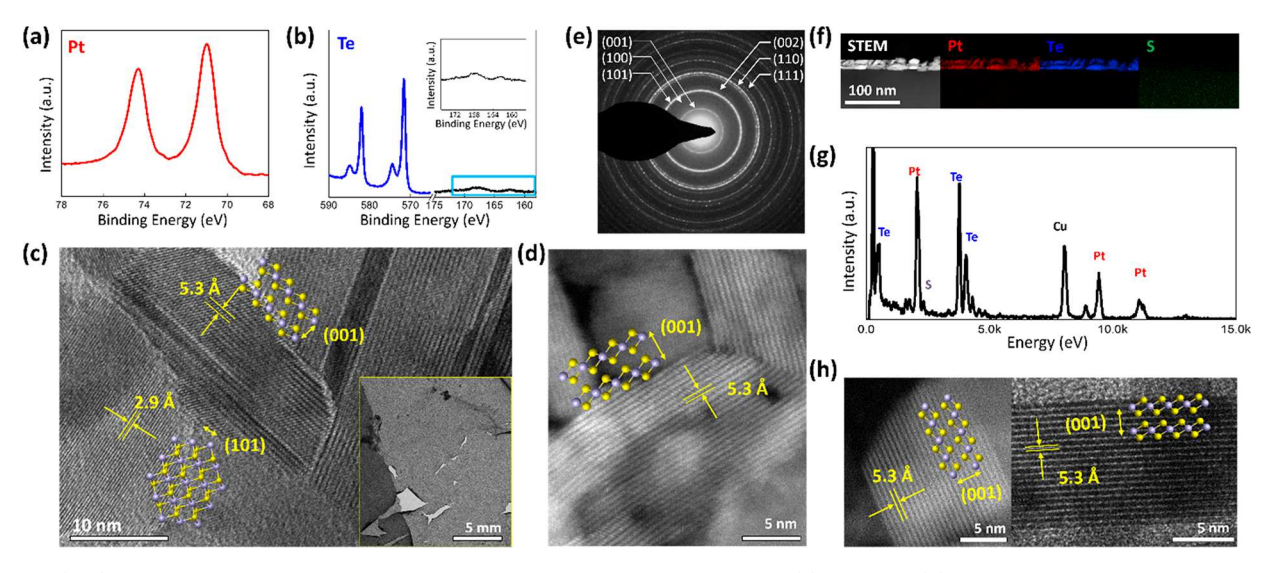


Figure 3. (a, b)hhhh XPS spectra of anion exchange-converted 2D PtTe<sub>2</sub> layers showing; (a) Pt 4f and (b) Te 3d core-level binding energies. The inset in (b) presents a magnified spectrum of the blue box for the S 2p core-level area. (c) Plane-view HR-TEM image of converted 2D PtTe<sub>2</sub> layers revealing mixed 2D layer orientations. The inset presents a low-magnification image of the TEM sample. (d) Plane-view HR-STEM image of converted 2D PtTe<sub>2</sub> layers revealing surface-exposed 2D vdW gaps. (e) SAED pattern indexing of converted 2D PtTe<sub>2</sub> layers. (f–h) Elemental mapping images (f), EDS spectrum (g), and (h) HR-TEM images obtained from a cross-sectioned sample of converted 2D PtTe<sub>2</sub> layers.

sectional EDS elemental mapping image obtained from the same sample in Figure 2a. The image confirms that the PtS film is  $\sim \! 10$  nm thick, constituting homogeneously distributed Pt and S atoms. The HR-STEM image in Figure 2e corresponding to Figure 2d visualizes (101) lattice fringes with a lattice spacing of 3.0 Å. The image well matches the atomic model of a tetragonal PtS crystal illustrated in Figure 2e, confirming its nonlayered 3D crystallinity. The EDS spectrum in Figure 2f obtained from the same cross-sectional TEM sample reveals the stoichiometric ratio of Pt:S  $\sim 55:45$ , consistent with the XPS analysis in Figure 2c as well as the previous study.  $^{31,33}$ 

Figure 3 depicts the structural and chemical properties of 2D PtTe2 vdW layers converted from the anion exchange of nonlayered 3D PtS thin films. Figure 3a,b present the corelevel XPS profiles of Pt and Te elements obtained from the converted 2D PtTe<sub>2</sub> layers. The XPS spectrum in Figure 3a exhibits Pt 4f core level peaks at 71.0 and 74.3 eV, which correspond to  $4f_{7/2}$  and  $4f_{5/2}$ , respectively. These binding energy values are similar to those observed from the previous studies on 2D PtTe<sub>2</sub> layers.<sup>35,36</sup> Likewise, the XPS spectrum in Figure 3b exhibits Te 3d core-level peaks at 574.5 and 585.0 eV corresponding to Te(IV) species as well as additional peaks corresponding to Te(0) at 571.6 and 582.0 eV, consistent with the previous observations with 2D PtTe<sub>2</sub> layers.<sup>35,36</sup> It is noteworthy that these Te-associated peaks are absent in the XPS characterization of initial PtS thin films before their conversion, correctly indicating the occurrence of S and Te anion exchange. Furthermore, it is remarkable to note that the S 2p peak intensity significantly decreased after the conversion, as presented in the zoomed-in spectrum in the inset corresponding to the blue box. The small amount of the S 2p peak presents residual S atoms trapped in the converted 2D PtTe<sub>2</sub> layers, which is verified by the EDS characterization in the later section. Figure 3c shows a representative plane-view HR-TEM image of converted 2D PtTe<sub>2</sub> layers. The measured lattice spacing of 5.3 Å matches the (001) lattice fringes of trigonal PtTe<sub>2</sub> crystals, <sup>17,19,37</sup> indicating that 2D layer edges are exposed on the surface, while the lattice spacing of 2.9 Å

corresponds to their (101) lattice fringes. The observation of such distinct 2D layer orientations confirms the presence of both horizontally and vertically aligned 2D layers in the sample, which is consistent with the atomic model presented in Figure 1a. The inset in Figure 3c shows a low-magnification TEM image of the same sample, exhibiting its large-area spatial homogeneity. Figure 3d shows a plane-view HR-STEM image that focuses on a grain of vertically aligned 2D PtTe<sub>2</sub> layers, revealing highly dense vdW gaps with a lattice spacing of 5.3 Å. Figure 3e exhibits indexed SAED patterns containing multiple rings that are quite distinct from those observed with the nonlayered PtS films before their conversion presented in Figure 2b. The indexed SAED ring patterns match the trigonal PtTe<sub>2</sub> crystalline structure with a space group of  $P\overline{3}m1$ ,  $^{17,19,37}$ which also confirms a mixture of vertically and horizontally aligned 2D layer orientations. In addition to the plane-view TEM analysis, cross-sectional TEM characterizations were performed to further clarify the structural and chemical properties of the converted 2D PtTe<sub>2</sub> layers. Figure 3f shows cross-sectional EDS elemental mapping images of 2D PtTe2 layers converted from PtS films, revealing a spatial distribution of constituting Pt, Te, and S atoms. While Pt and Te atoms are highly localized within the sample, the intensity of the S atoms is very weak and is nearly comparable to that of the background. Figure 3g presents the EDS spectrum obtained from the same sample revealing that the atomic ratio of Pt:Te is approximately ~30:66, which is a sharp contrast to the observation before the anion exchange conversion (Figure 2f). A small amount (i.e., typically <5% atomic ratio) of residual S atoms is detected within the sample, which is consistent with the XPS observation in Figure 3b. The cross-sectional HR-TEM images in Figure 3h show magnified views of the sample in Figure 3f, clearly revealing the presence of horizontally (left) and vertically (right) aligned 2D PtTe2 layers with a wellpreserved vdW gap spacing of 5.3 Å. All these comprehensive characterization data strongly suggest that the thermal anion exchange reaction at 400 °C successfully converts the nonlayered 3D PtS thin films into vdW PtTe2 layers with a mixed 2D layer orientation containing an insignificant amount

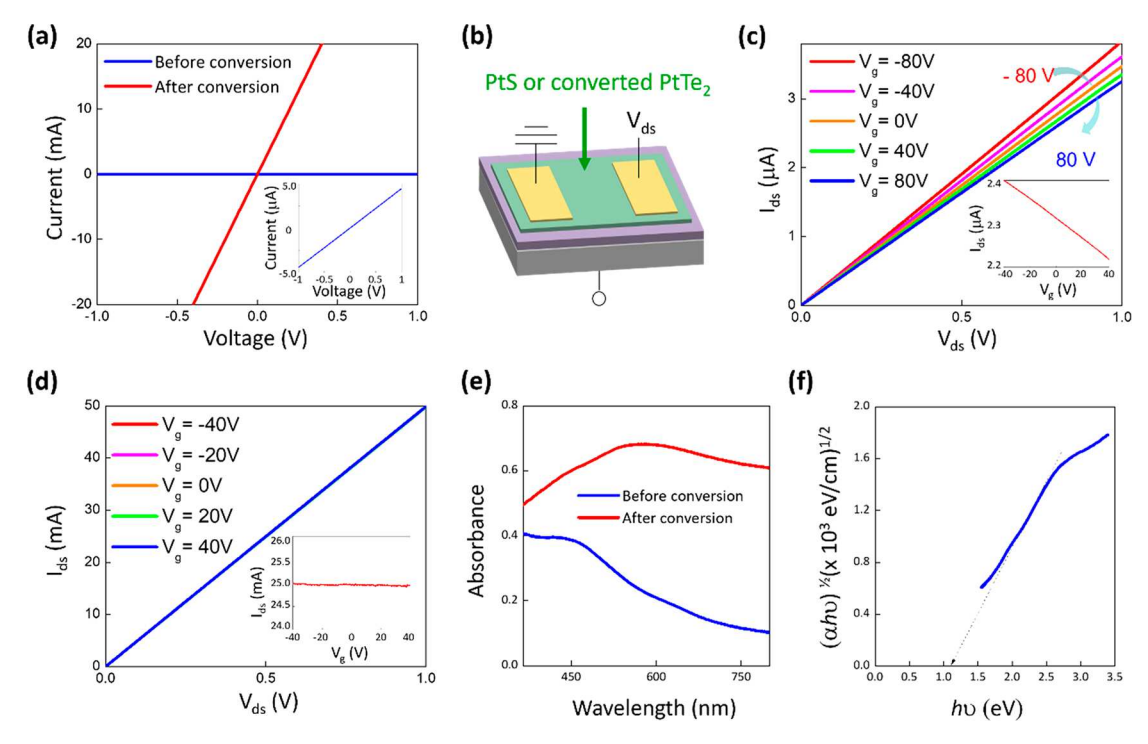


Figure 4. (a) I-V characteristics of a PtS thin film before (blue) and after (red) its conversion to 2D PtTe<sub>2</sub> layers. The inset shows a zoomed-in view of the I-V plot before the conversion, indicating that the electrical conductivity increases by >1000 times after the conversion. (b) Schematic illustration of a back-gated FET device adopting PtS or 2D PtTe<sub>2</sub> layers as the channel. (c) FET  $I_{ds}-V_{ds}$  transfer curve obtained from a PtS thin film indicating a p-type semiconducting transport. The inset shows the corresponding FET  $I_{ds}-V_g$  transfer curve. (d) FET  $I_{ds}-V_{ds}$  transfer curve obtained from converted 2D PtTe<sub>2</sub> layers indicating a highly metallic transport. The inset shows the corresponding FET  $I_{ds}-V_g$  transfer curve. (e) Optical absorbance spectra obtained from a PtS thin film grown on a glass substrate before (blue) and after (red) its conversion to 2D PtTe<sub>2</sub> layers. (f) Tauc plot converted from the optical absorbance of the preconverted PtS sample in (e).

of S atoms. In contrast to the mixture of vertical/horizontal 2D layer orientations in the samples converted from ~10 nm thick PtS films, we note that those converted from much thinner (~1.5 nm) films pronouncedly exhibit horizontally aligned 2D layers, as presented in Supporting Information, Figure S1. Furthermore, additional plane-view HR-TEM images of converted 2D PtTe<sub>2</sub> layers with mixed orientations reveal Moiré fringes and surface-exposed layer edges, confirming their intrinsic vdW layered structure (Supporting Information, Figure S2).

Having revealed the anion change exchange-driven structural and chemical conversion of the materials, we then investigated the tunability of their electrical properties accompanying the conversion. Figure 4a presents the current-voltage (I-V)characteristics obtained from the nonlayered 3D PtS thin film before conversion (blue line) and the converted 2D PtTe<sub>2</sub> layers (red line), respectively. It is interesting to note that the anion exchange conversion leads to a drastic increase of current by >1000 times; i.e., ~147 S/m for the PtS before the conversion and  $\sim 0.6 \times 10^6$  S/m for the 2D PtTe<sub>2</sub> after the conversion. In addition to the conductivity increase, this conversion process was identified to tune the carrier type of the materials as well. For this electrical characterization, fieldeffect transistors (FETs) were fabricated by employing both PtS film and converted 2D PtTe<sub>2</sub> layers as device channels. The FETs were in a back gate configuration with an identical channel dimension (width: 150  $\mu$ m, spacing: 50  $\mu$ m) defined by top gold (Au) electrodes, as illustrated in Figure 4b. Figure 4c,d exhibits the back-gate FET transfer characteristics of the PtS film and converted 2D PtTe<sub>2</sub> layers, respectively. Drainsource current  $(I_{ds})$  vs drain-source voltage  $(V_{ds})$  plots were

obtained with diverse amplitudes of back-gate voltage  $(V_{\sigma})$  for both devices. In Figure 4c, the PtS film before conversion displays p-type semiconducting characteristics manifested by the decrease of  $I_{ds}$  with increasing  $V_g$  from -80 to 80 V, consistent with the  $I_{ds}$ - $V_g$  transfer plot in the inset. On the other hand, the converted 2D PtTe2 layers exhibit completely overlapping  $I_{ds}$ – $V_{ds}$  plots regardless of varying  $V_{g}$  (Figure 4d), which is a signature of metallic characteristics. The corresponding inset shows a  $V_{\rm ds}$ -independent  $I_{\rm ds}$ - $V_{\rm g}$  transfer plot, further confirming the highly metallic nature of the converted material, which is consistent with our previous observations with pristine 2D PtTe<sub>2</sub> layers. <sup>19,38,39</sup> To further elucidate this conversion-driven semiconducting-to-metallic transition, we characterized the optical absorbance of a PtS sample prepared on a willow glass before/after its conversion using an ultraviolet-visible (UV-vis) spectroscopy. Figure 4e presents absorbance spectra of the sample before (blue line) and after (red line) the conversion, revealing absorbance intensities in the wavelength range of 350 to 800 nm. The intensity of the PtS steadily decreases with increasing wavelengths, consistent with previous studies, 30,40 while it significantly increases after the conversion to 2D PtTe2 layers. The distinct electrical properties of the sample realized by the anion exchange conversion—i.e., semiconducting-to-metallic transition in Figure 4c,d—were further investigated through optical characterization. Figure 4f presents the Tauc plot converted from the absorbance spectrum of the PtS thin film (Figure 4e, blue line), where  $\alpha$  is the optical absorption coefficient and hv is the photon energy. The optical bandgap of the sample is extracted to be  $\approx 1.1$  eV, similar to the values from previous studies, 30,40 which further confirms its semi-

conducting nature consistent with Figure 4c. The Tauc plot of the 2D PtTe<sub>2</sub> layers converted from the PtS thin film is also presented in Supporting Information, Figure S3, comparing absorbance characteristics before/after the anion exchange reaction.

The underlying thermodynamic principle for the anion exchange-driven conversion of PtS to 2D PtTe<sub>2</sub> layers was examined by the DFT-based first-principles calculations. The phonon band structures of bulk PtS and 2D PtTe<sub>2</sub> layers were calculated using the matrix of second derivatives of the energy with respect to atomic displacements. Figure 5a,b presents the

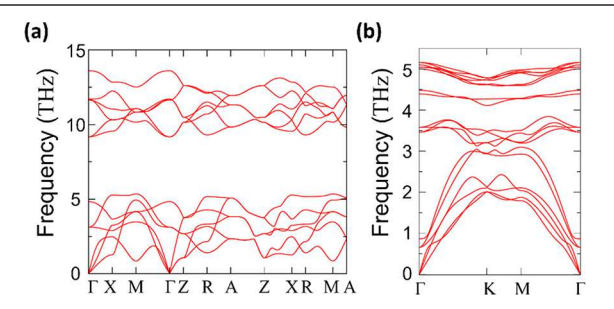


Figure 5. Phonon band structures for (a) bulk PtS and (b) 2D PtTe<sub>2</sub> layers, confirming both materials exhibit positive phonon frequencies.

calculation results for the PtS and 2D PtTe<sub>2</sub> layers, respectively, showing positive frequency values for both materials, confirming their dynamical stability. The following reaction equation for the anion exchange conversion was employed;

$$PtS + 2Te(gas) \rightarrow PtTe_2 + S(gas)$$

For the calculation of the Gibbs free energies of bulk PtS and 2D PtTe<sub>2</sub> layers, we incorporated the thermal correction determined by the experimental growth conditions (i.e., temperature = 400 °C and pressure = 50 mTorr) into the corresponding free energies at 0 K. The free energies of single Te and S atoms (in the gas phase, noted above) were considered in our simulations as well (see the computational details in the Experimental Section). We identified that the total energy of the products is smaller than that of the reactants—i.e., Gibbs free energy change,  $\Delta G = -1.71$  eV, which leads to the conclusion that this anion exchange conversion is thermodynamically favorable. We note that this reaction is an oxidation-reduction (redox) reaction in which Te acts as an oxidizing agent, whereas PtS is a reducing agent. Details about reaction energetics and dynamics are provided in the DFT simulation section in the Supporting Information.

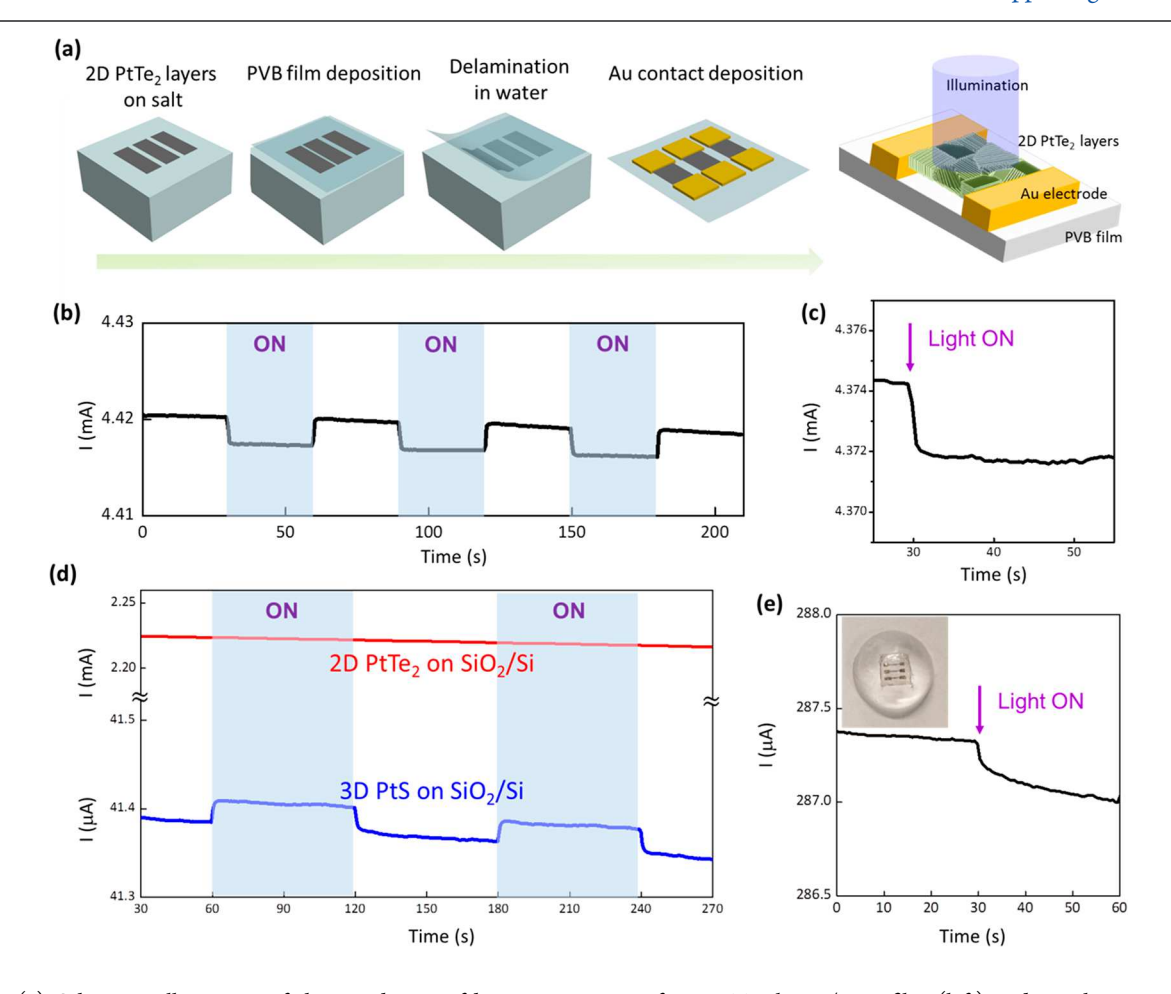


Figure 6. (a) Schematic illustration of the step-by-step fabrication process of 2D PtTe<sub>2</sub> layers/PVB film (left) and its photoresponsiveness measurement scheme (right). (b) Temporal photoresponsiveness obtained under 625 nm illumination with 20 mW/cm<sup>2</sup> intensity. (c) Temporal photoresponsiveness obtained under 940 nm illumination with 118 mW/cm<sup>2</sup> intensity. (d) Temporal photoresponsiveness characteristics obtained from samples of 2D PtTe<sub>2</sub> on  $SiO_2/Si$  (red plot) and PtS on  $SiO_2/Si$  (blue plot), respectively. (e) Temporal photoresponsiveness obtained from a sample of 2D PtTe<sub>2</sub> layers/PVB film integrated on a hemispherical PDMS, measured under 625 nm illumination with 25.3 mW/cm<sup>2</sup> intensity. All the measurements in (b)–(e) were performed at a bias voltage of 500 mV.

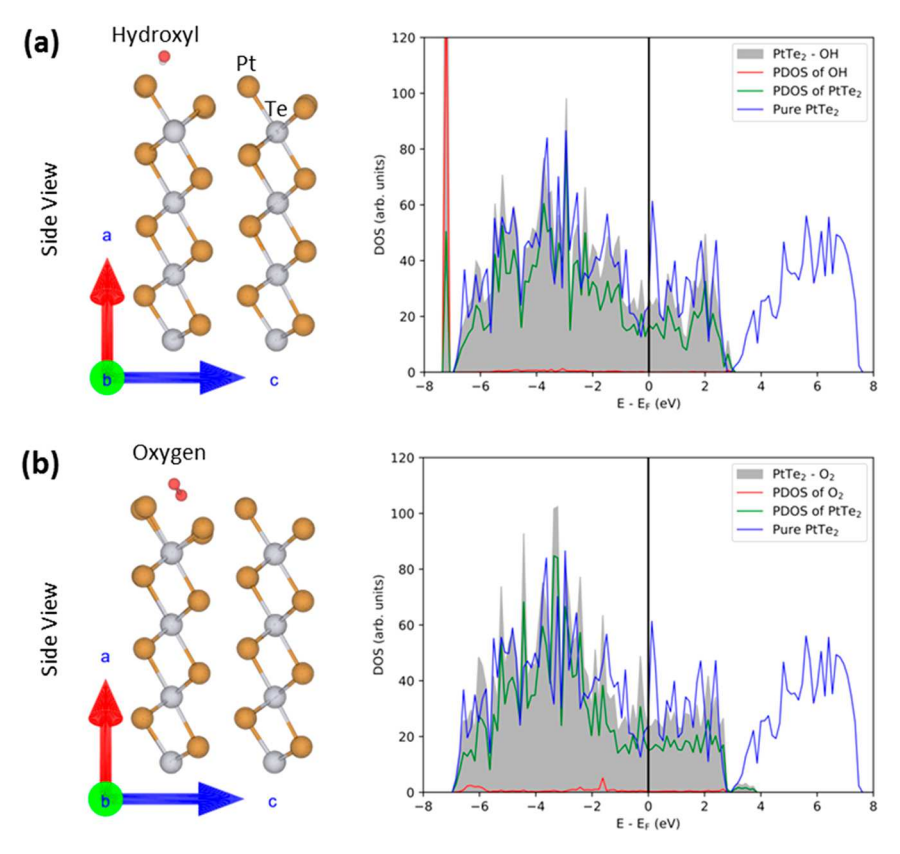


Figure 7. DOS and PDOS of vertically aligned 2D PtTe<sub>2</sub> bilayers affected by (a) OH and (b) O<sub>2</sub> adsorbate attachment.

Having confirmed the anion exchange-driven structural/ electrical transition as well as its underlying principle, we then explored application opportunities of the converted 2D PtTe<sub>2</sub> layers utilizing their optoelectronic properties. Specifically, we focused on unveiling their unusual negative photoresponsiveness—i.e., photocurrent decrease upon optical illumination by integrating them on polymeric substrates. Figure 6a illustrates the step-by-step fabrication process for 2D PtTe<sub>2</sub> layers/polymer photoresponsive devices where PVB  $((C_8H_{14}O_2)_n)$  is used as the polymer substrate. The first step includes the preparation of PtS thin films on a single crystalline salt wafer (sodium chloride, NaCl) and their subsequent anion exchange conversion to 2D PtTe2 layers. Then, a dispersion of PVB is drop-casted on top of the converted 2D PtTe<sub>2</sub> layers/ salt wafer, which is subsequently spin-coated followed by curing at room temperature. Details regarding the PVB preparation are presented in the Experimental Section. Next, the PVB-integrated 2D PtTe<sub>2</sub> layers/salt wafer is slowly dipped into deionized (DI) water, which allows for the delamination of the 2D PtTe2 layer-attached PVB film from the wafer. The delamination is enabled by the high-water solubility of the salt wafer as verified in our previous work.<sup>37</sup> Gold (Au) top electrode contacts are subsequently deposited on top of the 2D PtTe<sub>2</sub> layers/PVB film for photoresponsiveness measurements. The schematic illustration on the right panel in Figure 6a shows the experimental setup used to illuminate and characterize the photoresponsiveness of the 2D PtTe2 layers/ PVB film. Figure 6b presents temporal characteristics of photoresponsiveness under a visible 625 nm optical illumination with 20 mW/cm<sup>2</sup> intensity, measured at a bias voltage of 500 mV. It is interesting to observe a pronounced negative photoresponsiveness—i.e., current decrease upon illumina-

tion—which is well retained under the periodically applied illumination. The negative photoresponsiveness was also confirmed under near-infrared (NIR) illumination at 940 nm, as presented in Figure 6c. Responsivity, R, is defined as I  $I_{\rm ph} | \times \hat{P}_{\rm in}^{-1}$  where  $I_{\rm ph}$  and  $P_{\rm in}$  are photocurrent and incident optical power, respectively, and it quantizes the sensitivity of a photodetector. <sup>22,41</sup> The negative photoconductive responsivity is calculated to be 0.805 mA/W for the visible wavelength (625 nm) and 0.115 mA/W for the NIR wavelength (940 nm), respectively. For comparison, we performed control experiments of photoresponsiveness measurements using anion exchange-converted 2D PtTe2 layers as well as PtS films, both of which were integrated on SiO<sub>2</sub>/Si substrates. Figure 6d clearly shows that the 2D PtTe2 on SiO2/Si (red plot) does not exhibit any noticeable negative photoresponsiveness while the PtS film exhibits positive photoresponsiveness. The results confirm that the negative photoresponsiveness observed with the 2D PtTe<sub>2</sub> layers/PVB sample must be attributed to the presence of the PVB substrate. In other words, it is assumed that the PVB substrate interfaced with 2D PtTe<sub>2</sub> layers plays a critical role in altering their intrinsic charge trapping characteristics. In fact, it has been reported that the photoinduced change of adsorbate (e.g., O<sub>2</sub>/OH)-related impurity states at 2D materials/polymer interfaces can significantly affect the density of charge carriers in 2D materials.<sup>24</sup> Such defect-driven electronic structure variations are therefore responsible for giving rise to negative photoresponsiveness as observed in graphene interfaced with poly(methyl methacrylate) (PMMA) systems.<sup>24</sup> The mechanical flexibility of 2D PtTe2 layers/PVB films further allows their direct integration onto unconventional substrates with uneven surfaces. Figure 6e presents negative photoresponsiveness

obtained from the sample integrated onto hemispherical polydimethylsiloxane (PDMS) (inset image). The measurement was performed at 625 nm illumination with an intensity of 25.3 mW/cm<sup>2</sup> at a bias voltage of 500 mV, yielding a negative photoconductive responsivity of 6.206  $\mu$ A/W.

To clarify the origin of the negative photoresponsiveness, we employed DFT calculations and investigated possible effects of the adsorbates on the electronic structure of 2D PtTe<sub>2</sub> layers. Figure 7 presents the electronic density of states (DOS) and atomic projected density of states (PDOS) of vertically aligned 2D PtTe2 bilayers, where two different adsorbates of OH and O<sub>2</sub> are attached (Figure 7a,b, respectively). The unit cell consists of one adsorbate and two layers of PtTe2 with a vacuum of ~15 Å thickness added in the vertical direction to remove spurious interaction between periodic images. The vdW interaction is taken account by using the DFT-D3 method with Becke-Johnson damping (DFT-D3(BJ)),<sup>42</sup> and effects of spin-orbit coupling are not considered in our calculations. A gamma-centered k-point  $1 \times 6 \times 6$  mesh is used for structural relaxation and for the self-consistent calculations of the first Brillouin zone sampling. DOS and PDOS were extracted using the VASPKIT program and were plotted using the Matplotlib software, 43,44 and the visualization of the system was prepared by VESTA.45 To be consistent with the experimental setting of 2D PtTe2 layers/PVB films, we focused our calculations on revealing how OH and O2 on the edges of vertically aligned 2D PtTe2 layers affect their electronic structures. Figure 7a shows that OH groups introduce highly localized states within the band structure of 2D PtTe2 layers near its Fermi level ( $E < E_F$ ). Such localized states can act as scattering centers enabling the significant trapping of free electrons under light illumination leading to negative photoresponsiveness, as previously observed with graphene.<sup>24</sup> Meanwhile, O2 does not introduce any significant change in the localized states (Figure 7b), which indicates the alternation of the band structure is adsorbate-sensitive. While the analysis was limited to the two model systems of OH and O2, it strongly suggests that the light-induced trapping/detrapping of free electrons is highly feasible with a variety of adsorbates.

# 4. CONCLUSIONS

In summary, we observed a chemical and structural conversion of nonlayered 3D PtS to layered vdW 2D PtTe<sub>2</sub> via a controlled CVD tellurization at 400 °C. This anion exchange conversion also led to the precise tuning of resulting electrical and optical properties; i.e., semiconducting-to-metallic transition and drastic increase in optical absorbance. DFT calculations employing the energy landscape of the adopted tellurization process confirmed the thermodynamic stability of this anion exchange reaction. Lastly, the converted 2D PtTe<sub>2</sub> layers integrated onto PVB exhibited negative photoresponsiveness, opposite to the characteristics observed with 2D PtTe<sub>2</sub> layers integrated on SiO<sub>2</sub>/Si.

# ASSOCIATED CONTENT

#### Supporting Information

The Supporting Information is available free of charge at https://pubs.acs.org/doi/10.1021/acs.chemmater.2c01452.

Cross-sectional HR-TEM and EDS mapping images of converted 2D PtTe<sub>2</sub> layers showing horizontally aligned layers, plane-view HR-TEM images of converted 2D PtTe<sub>2</sub> layers showing Moiré fringes and surface-exposed

layer edges, Tauc plots of the PtS thin film before and after its anion exchange conversion, and DFT calculation parameter and equation details (PDF)

### AUTHOR INFORMATION

# **Corresponding Authors**

Yeonwoong Jung — NanoScience Technology Center,
Department of Electrical and Computer Engineering, and
Department of Materials Science and Engineering, University
of Central Florida, Orlando, Florida 32826, United States;
orcid.org/0000-0001-6042-5551;

Email: yeonwoong.jung@ucf.edu

Jung Han Kim — Department of Materials Science and Engineering, Dong-A University, Busan 49315, South Korea; orcid.org/0000-0002-6678-2282; Email: junghankim@dau.ac.kr

#### **Authors**

Sang Sub Han – NanoScience Technology Center, University of Central Florida, Orlando, Florida 32826, United States

Mashiyat Sumaiya Shawkat — NanoScience Technology Center and Department of Electrical and Computer Engineering, University of Central Florida, Orlando, Florida 32826, United States

Yoong Hee Lee – Department of Chemistry, Seoul National University, Seoul 08826, South Korea

Gyehyun Park – Department of Chemistry, Seoul National University, Seoul 08826, South Korea; ⊙ orcid.org/0000-0001-7554-713X

**Hao Li** – NanoScience Technology Center, University of Central Florida, Orlando, Florida 32826, United States

**Hee-Suk Chung** – Analytical Research Division, Korea Basic Science Institute, Jeonju 54907, South Korea

Changhyeon Yoo – NanoScience Technology Center, University of Central Florida, Orlando, Florida 32826, United States

Sohrab Alex Mofid – NanoScience Technology Center, University of Central Florida, Orlando, Florida 32826, United States

Shahid Sattar — Department of Physics and Electrical Engineering, Linnaeus University, Kalmar SE-39231, Sweden; orcid.org/0000-0003-4409-0100

Nitin Choudhary - NanoScience Technology Center, University of Central Florida, Orlando, Florida 32826, United States

Jea-Young Choi − Department of Materials Science and Engineering, Dong-A University, Busan 49315, South Korea YounJoon Jung − Department of Chemistry, Seoul National University, Seoul 08826, South Korea; orcid.org/0000-0002-9464-9999

Complete contact information is available at: https://pubs.acs.org/10.1021/acs.chemmater.2c01452

### **Author Contributions**

S.S.H. and M.S.S. prepared the samples, conducted anion exchange reactions, and performed optical and electrical measurements with the assistance of C.Y. and S.A.M. under the guidance of Y.J. J.-Y.C. and J.H.K. performed a majority of the structural and chemical characterization experiments as well as associated data interpretations. H.-S.C. participated in TEM experiments. H.L. and N.C. participated in manuscript writing and data analysis. S.S. performed DFT calculations for

the phonon band. Y.H.L. and G.P. performed DFT calculations for the adsorbate system under the supervision of Y.J. (SNU). S.S.H. and Y.J. wrote the manuscript with inputs from all authors.

#### Notes

The authors declare no competing financial interest.

#### ACKNOWLEDGMENTS

Y.J. acknowledges financial support from the National Science Foundation (CAREER: CMMI-2142310), the University of Central Florida (VPR Advancement of Early Career Researchers award), and the Korea Institute of Energy Technology Evaluation and Planning (KETEP) (No. 20173010013340). J.H.Kim was supported by the Commercialization Promotion Agency for R&D Outcomes (COMPA) funded by the Ministry of Science and ICT (MSIT) (06-1, Development of Core Technology for Future Leading Research Equipment). S.S. thanks Carl Tryggers Stiftelsen (CTS 20:71) for financial support. The computations were enabled by resources provided by the Swedish National Infrastructure for Computing (SNIC) at HPC2N and NSC partially funded by the Swedish Research Council through Grant Agreement No. 2018-05973. The work at SNU was supported by the National Research Foundation of Korea (NRF-2018R1D1A1B07043973).

### REFERENCES

- (1) Wang, Q. H.; Kalantar-Zadeh, K.; Kis, A.; Coleman, J. N.; Strano, M. S. Electronics and Optoelectronics of Two-Dimensional Transition Metal Dichalcogenides. *Nat. Nanotechnol* **2012**, *7* (11), 699–712.
- (2) Bonaccorso, F.; Colombo, L.; Yu, G.; Stoller, M.; Tozzini, V.; Ferrari, A. C.; Ruoff, R. S.; Pellegrini, V. Graphene, Related Two-Dimensional Crystals, and Hybrid Systems for Energy Conversion and Storage. *Science* **2015**, 347 (6217), 1246501.
- (3) Zhang, X.; Lai, Z.; Tan, C.; Zhang, H. Solution-processed Two-dimensional MoS<sub>2</sub> Nanosheets: Preparation, Hybridization, and Applications. *Angew. Chem. Int. Ed* **2016**, *55* (31), 8816–8838.
- (4) Ko, T.-J.; Wang, M.; Yoo, C.; Okogbue, E.; Islam, M. A.; Li, H.; Shawkat, M. S.; Han, S. S.; Oh, K. H.; Jung, Y. Large-area 2D TMD layers for mechanically reconfigurable electronic devices. *J. Phys. D Appl. Phys.* **2020**, *53*, 313002.
- (\$\tilde{5}\$) Han, S. S.; Ko, T.-J.; Yoo, C.; Shawkat, M. S.; Li, H.; Kim, B. K.; Hong, W.-K.; Bae, T.-S.; Chung, H.-S.; Oh, K. H.; et al. Automated Assembly of Wafer-Scale 2D TMD Heterostructures of Arbitrary Layer Orientation and Stacking Sequence Using Water Dissoluble Salt Substrates. *Nano Lett.* **2020**, 20 (\$\tilde{5}\$), 3925-3934.
- (6) Wang, M.; Li, H.; Ko, T.-J.; Shawkat, M. S.; Okogbue, E.; Yoo, C.; Han, S. S.; Islam, M. A.; Oh, K. H.; Jung, Y. Manufacturing Strategies for Wafer-scale Two-dimensional Transition Metal Dichalcogenide Heterolayers. *J. Mater. Res.* **2020**, *35* (11), 1350–1368.
- (7) Lee, Y. H.; Zhang, X. Q.; Zhang, W.; Chang, M. T.; Lin, C. T.; Chang, K. D.; Yu, Y. C.; Wang, J. T. W.; Chang, C. S.; Li, L. J.; et al. Synthesis of Large-area MoS<sub>2</sub> Atomic Layers with Chemical Vapor Deposition. *Adv. Mater.* **2012**, 24 (17), 2320–2325.
- (8) Liu, K.-K.; Zhang, W.; Lee, Y.-H.; Lin, Y.-C.; Chang, M.-T.; Su, C.-Y.; Chang, C.-S.; Li, H.; Shi, Y.; Zhang, H.; et al. Growth of Large-Area and Highly Crystalline MoS<sub>2</sub> Thin Layers on Insulating Substrates. *Nano Lett.* **2012**, *12* (3), 1538–1544.
- (9) Son, D. H.; Hughes, S. M.; Yin, Y.; Alivisatos, A. P.; et al. Cation Exchange Reactions in Ionic Nanocrystals. *science* **2004**, *306* (5698), 1009–1012.
- (10) Agarwal, R.; Krook, N. M.; Ren, M.-L.; Tan, L. Z.; Liu, W.; Rappe, A. M.; Agarwal, R. Anion Exchange in II-VI Semiconducting

- Nanostructures via Atomic Templating. *Nano Lett.* **2018**, *18* (3), 1620–1627.
- (11) Steimle, B. C.; Fenton, J. L.; Schaak, R. E. Rational Construction of a Scalable Heterostructured Nanorod Megalibrary. *Science* **2020**, *367* (6476), 418–424.
- (12) Tang, J.; Huo, Z.; Brittman, S.; Gao, H.; Yang, P. Solution-processed Core—shell Nanowires for Efficient Photovoltaic Cells. *Nat. Nanotechnol* **2011**, *6* (9), 568–572.
- (13) Chen, H.; Cao, C.; Ge, B.; Li, Y.; Han, J.; Chen, Z. Wafer-scale Metal Chalcogenide Thin Films via An Ion Exchange Approach. *J. Mater. Chem. C* **2020**, *8* (41), 14393–14401.
- (14) Chen, H.; Chen, Z.; Ge, B.; Chi, Z.; Chen, H.; Wu, H.; Cao, C.; Duan, X. General Strategy for Two-Dimensional Transition Metal Dichalcogenides by Ion Exchange. *Chem. Mater.* **2017**, *29* (23), 10019–10026.
- (15) Yun, S. J.; Han, G. H.; Kim, H.; Duong, D. L.; Shin, B. G.; Zhao, J.; Vu, Q. A.; Lee, J.; Lee, S. M.; Lee, Y. H. Telluriding Monolayer MoS<sub>2</sub> and WS<sub>2</sub> via Alkali Metal Scooter. *Nat. Commun.* **2017**, 8 (1), 2163.
- (16) Fu, L.; Hu, D.; Mendes, R. G.; Rümmeli, M. H.; Dai, Q.; Wu, B.; Fu, L.; Liu, Y. Highly Organized Epitaxy of Dirac Semimetallic PtTe<sub>2</sub> Crystals with Extrahigh Conductivity and Visible Surface Plasmons at Edges. *ACS Nano* **2018**, *12* (9), 9405–9411.
- (17) Li, X.; Fan, Y. J.; Li, H. Y.; Cao, J. W.; Xiao, Y. C.; Wang, Y.; Liang, F.; Wang, H. L.; Jiang, Y.; Wang, Z. L.; Zhu, G. Ultracomfortable Hierarchical Nanonetwork for Highly Sensitive Pressure Sensor. ACS Nano 2020, 14 (8), 9605–9612.
- (18) Ma, H.; Chen, P.; Li, B.; Li, J.; Ai, R.; Zhang, Z.; Sun, G.; Yao, K.; Lin, Z.; Zhao, B.; Wu, R.; Tang, X.; Duan, X.; Duan, X. Thickness-Tunable Synthesis of Ultrathin Type-II Dirac Semimetal PtTe<sub>2</sub> Single Crystals and Their Thickness-Dependent Electronic Properties. *Nano Lett.* **2018**, *18* (6), 3523–3529.
- (19) Ko, T.-J.; Han, S. S.; Okogbue, E.; Shawkat, M. S.; Wang, M.; Ma, J.; Bae, T.-S.; Hafiz, S. B.; Ko, D.-K.; Chung, H.-S.; Oh, K. H.; Jung, Y. Wafer-scale 2D PtTe<sub>2</sub> layers-enabled Kirigami heaters with superior mechanical stretchability and electro-thermal responsiveness. *Appl. Mater. Today* **2020**, *20*, 100718.
- (20) Villaos, R. a. B.; Crisostomo, C. P.; Huang, Z.-Q.; Huang, S.-M.; Padama, A. a. B.; Albao, M. A.; Lin, H.; Chuang, F.-C. Thickness Dependent Electronic Properties of Pt Dichalcogenides. *NPJ. 2D Mater. Appl.* **2019**, 3 (1), 2.
- (21) Lin, M.-K.; Villaos, R. a. B.; Hlevyack, J. A.; Chen, P.; Liu, R.-Y.; Hsu, C.-H.; Avila, J.; Mo, S.-K.; Chuang, F.-C.; Chiang, T. C. Dimensionality-Mediated Semimetal-Semiconductor Transition in Ultrathin PtTe, Films. *Phys. Rev. Lett.* **2020**, *124* (3), 036402.
- (22) Shawkat, M. S.; Chowdhury, T. A.; Chung, H.-S.; Sattar, S.; Ko, T.-J.; Larsson, J. A.; Jung, Y. Large-area 2D PtTe<sub>2</sub>/silicon Vertical-Junction Devices with Ultrafast and High-sensitivity Photodetection and Photovoltaic Enhancement by Integrating Water Droplets. *Nanoscale* **2020**, *12* (45), 23116–23124.
- (23) Shawkat, M. S.; Hafiz, S. B.; Islam, M. M.; Mofid, S. A.; Al Mahfuz, M. M.; Biswas, A.; Chung, H.-S.; Okogbue, E.; Ko, T.-J.; Chanda, D.; Roy, T.; Ko, D.-K.; Jung, Y. Scalable Van der Waals Two-Dimensional PtTe<sub>2</sub> Layers Integrated onto Silicon for Efficient Nearto-Mid Infrared Photodetection. *ACS Appl. Mater. Interfaces* **2021**, *13* (13), 15542–15550.
- (24) Biswas, C.; Gunes, F.; Loc, D. D.; Lim, S. C.; Jeong, M. S.; Pribat, D.; Lee, Y. H. Negative and Positive Persistent Photoconductance in Graphene. *Nano Lett.* **2011**, *11* (11), 4682–4687.
- (25) Blochl, P. E. Projector Augmented-Wave Method. Phys. Rev. B Condens Matter 1994, 50 (24), 17953-17979.
- (26) Kresse, G.; FurthmüLler, J. Efficient Iterative Schemes for ab Initio Total-Energy Calculations Using a Plane-Wave Basis Set. *Phys. Rev. B* **1996**, *54* (16), 11169–11186.
- (27) Kresse, G.; Joubert, D. From Ultrasoft Pseudopotentials to the Projector Augmented-Wave Method. *Phys. Rev. B* **1999**, *59* (3), 1758–1775.
- (28) Togo, A.; Tanaka, I. First Principles Phonon Calculations in Materials Science. Scr Mater. 2015, 108, 1–5.

- (29) Bendavid, L. I.; Carter, E. A. CO<sub>2</sub> Adsorption on Cu<sub>2</sub>O(111): A DFT+U and DFT-D Study. *J. Phys. Chem. C* **2013**, *117* (49), 26048–26059
- (30) Huang, J.; Dong, N.; Mcevoy, N.; Wang, L.; Coileain, C. O.; Wang, H.; Cullen, C. P.; Chen, C.; Zhang, S.; Zhang, L.; Wang, J. Surface-State Assisted Carrier Recombination and Optical Nonlinearities in Bulk to 2D Nonlayered PtS. ACS Nano 2019, 13 (11), 13390–13402.
- (31) Rozhdestvina, V. I.; Udovenko, A. A.; Rubanov, S. V.; Mudrovskaya, N. V. Structural Investigation of Cooperite (PtS) Crystals. *Crystallogr. Rep* **2016**, *61* (2), 193–202.
- (32) Marmier, A.; Ntoahae, P. S.; Ngoepe, P. E.; Pettifor, D. G.; Parker, S. C. Negative Compressibility in Platinum Sulfide using Density-Functional Theory. *Phys. Rev. B* **2010**, *81* (17), 172102–172105.
- (33) Han, S. S.; Ko, T. J.; Shawkat, M. S.; Shum, A. K.; Bae, T. S.; Chung, H. S.; Ma, J.; Sattar, S.; Hafiz, S. B.; Mahfuz, M. M. A.; Mofid, S. A.; Larsson, J. A.; Oh, K. H.; Ko, D. K.; Jung, Y. Peel-and-Stick Integration of Atomically Thin Nonlayered PtS Semiconductors for Multidimensionally Stretchable Electronic Devices. *ACS Appl. Mater. Interfaces* **2022**, *14* (17), 20268–20279.
- (34) Dembowski, J.; Marosi, L.; Essig, M. Platinum Sulfide by XPS. Surf. Sci. Spectra 1993, 2 (2), 104–108.
- (35) Kireev, D.; Okogbue, E.; Jayanth, R. T.; Ko, T.-J.; Jung, Y.; Akinwande, D. Multipurpose and Reusable Ultrathin Electronic Tattoos Based on PtSe<sub>2</sub> and PtTe<sub>2</sub>. ACS Nano **2021**, 15 (2), 2800–2811
- (36) Politano, A.; Chiarello, G.; Kuo, C.-N.; Lue, C. S.; Edla, R.; Torelli, P.; Pellegrini, V.; Boukhvalov, D. W. Tailoring the Surface Chemical Reactivity of Transition-Metal Dichalcogenide PtTe<sub>2</sub> Crystals. *Adv. Funct Mater.* **2018**, 28 (15), 1706504–1706511.
- (37) Shawkat, M. S.; Gil, J.; Han, S. S.; Ko, T. J.; Wang, M.; Dev, D.; Kwon, J.; Lee, G. H.; Oh, K. H.; Chung, H. S.; Roy, T.; Jung, Y.; Jung, Y. Thickness-Independent Semiconducting-to-Metallic Conversion in Wafer-Scale Two-Dimensional PtSe<sub>2</sub> Layers by Plasma-Driven Chalcogen Defect Engineering. ACS Appl. Mater. Interfaces 2020, 12 (12), 14341–14351.
- (38) Wang, M.; Ko, T.-J.; Shawkat, M. S.; Han, S. S.; Okogbue, E.; Chung, H.-S.; Bae, T.-S.; Sattar, S.; Gil, J.; Noh, C.; Oh, K. H.; Jung, Y.; Larsson, J. A.; Jung, Y. Wafer-Scale Growth of 2D PtTe<sub>2</sub> with Layer Orientation Tunable High Electrical Conductivity and Superior Hydrophobicity. ACS Appl. Mater. Interfaces **2020**, 12 (9), 10839–10851
- (39) Okogbue, E.; Ko, T.-J.; Han, S. S.; Shawkat, M. S.; Wang, M.; Chung, H.-S.; Oh, K. H.; Jung, Y. Wafer-scale 2D PtTe<sub>2</sub> layers for high-efficiency mechanically flexible electro-thermal smart window applications. *Nanoscale* **2020**, *12* (19), 10647–10655.
- (40) Shawkat, M. S.; Han, S. S.; Chung, H. S.; Mofid, S. A.; Yoo, C.; Jung, Y. Wafer-Scale Van der Waals Assembly of Free-Standing Near Atom Thickness Hetero-Membranes for Flexible Photo-Detectors. *Adv. Electron Mater.* **2021**, *7* (8), 2100395.
- (41) Konstantatos, G. Current Status and Technological Prospect of Photodetectors Based on Two-Dimensional Materials. *Nat. Commun.* **2018**, 9 (1), 5266.
- (42) Grimme, S.; Ehrlich, S.; Goerigk, L. Effect of the Damping Function in Dispersion Corrected Density Functional Theory. *J. Comput. Chem.* **2011**, 32 (7), 1456–65.
- (43) Wang, V.; Xu, N.; Liu, J.-C.; Tang, G.; Geng, W.-T. VASPKIT: A User-Friendly Interface Facilitating High-Throughput Computing and Analysis Using VASP Code. *Comput. Phys. Commun.* **2021**, 267, 108033.
- (44) Hunter, J. D. Matplotlib: A 2D Graphics Environment. *Comput. Sci. Eng.* **2007**, 9 (3), 90–95.
- (45) Momma, K.; Izumi, F. VESTA 3 for Three-Dimensional Visualization of Crystal, Volumetric and Morphology Data. *J. Appl. Crystallogr.* **2011**, 44 (6), 1272–1276.

# **□** Recommended by ACS

Phase Transition-Induced Temperature-Dependent Phonon Shifts in Molybdenum Disulfide Monolayers Interfaced with a Vanadium Dioxide Film

A.-Rang Jang, Woong-Ki Hong, et al.

JANUARY 07, 2021

ACS APPLIED MATERIALS & INTERFACES

READ 🗹

Doping Concentration Modulation in Vanadium-Doped Monolayer Molybdenum Disulfide for Synaptic Transistors

Jingyun Zou, Hui-Ming Cheng, et al.

MARCH 25, 2021

ACS NANO

READ 🗹

Fabrication of Epitaxial W-Doped  ${\rm VO}_2$  Nanostructured Films for Terahertz Modulation Using the Solvothermal Process

Alexey V. Ivanov, Olga V. Boytsova, et al.

OCTOBER 08, 202

ACS APPLIED NANO MATERIALS

READ 🗹

Formation of Uniquely Oriented VO $_2$  Thin Films by Topotactic Oxidation of V $_2$ O $_3$  Epitaxial Films on R-Plane  $Al_2$ O $_3$ 

Yuya Matamura, Tetsuji Hirato, et al.

APRIL 12, 2022

CRYSTAL GROWTH & DESIGN

READ 🗹

Get More Suggestions >